Inviscid criterion for decomposing scales

Dongxiao Zhao* and Hussein Aluie
Department of Mechanical Engineering and Laboratory for Laser Energetics, University of Rochester, Rochester, New York 14627, USA

(Received 8 November 2017; published 4 May 2018)

The proper scale decomposition in flows with significant density variations is not as straightforward as in incompressible flows, with many possible ways to define a "length scale." A choice can be made according to the so-called *inviscid criterion* [Aluie, Physica D **24**, 54 (2013)]. It is a kinematic requirement that a scale decomposition yield negligible viscous effects at large enough length scales. It has been proved [Aluie, Physica D **24**, 54 (2013)] recently that a Favre decomposition satisfies the inviscid criterion, which is necessary to unravel inertial-range dynamics and the cascade. Here we present numerical demonstrations of those results. We also show that two other commonly used decompositions can violate the inviscid criterion and, therefore, are not suitable to study inertial-range dynamics in variable-density and compressible turbulence. Our results have practical modeling implication in showing that viscous terms in Large Eddy Simulations do not need to be modeled and can be neglected.

DOI: 10.1103/PhysRevFluids.3.054603

I. INTRODUCTION

The notion of a "length scale" in a fluid flow does not exist as an independent entity but is associated with the specific flow variable being analyzed [1]. While this might seem obvious, we often discuss the "inertial range" or the "viscous range" of length scales in turbulence as if they exist independently of a flow variable, which in incompressible turbulence is the velocity field as Kolmogorov showed [2]. The overarching theme of this paper pertains to the following question: *Can an inertial-range exist for one quantity but not another within the same flow?* The answer is *yes*. Herring *et al.* [3] studied the dynamics of a passive scalar, $\theta(\mathbf{x})$, advected by an incompressible turbulent velocity, $\mathbf{u}(\mathbf{x})$, and showed that potential vorticity, $(\boldsymbol{\nabla}\times\mathbf{u})\cdot\boldsymbol{\nabla}\theta$, which is an ideal Lagrangian invariant, does not have an inertial range [4]. This is despite the existence of an inertial range for each of $\mathbf{u}$ and θ. They showed that this is due to significant viscous contributions to the evolution of $(\boldsymbol{\nabla}\times\mathbf{u})\cdot\boldsymbol{\nabla}\theta$ at *all* length scales, thereby precluding the existence of an inertial range.

In turbulent flows where significant density variations exist, we will show here that a similar situation can occur. In such flows, ascribing a length scale to momentum or kinetic energy is not as straightforward as in incompressible flows. Such quantities are one order higher in nonlinearity compared to their incompressible counterparts due to the density field. This has led to different scale decompositions being used in the literature. The length scale within these different decompositions corresponds to different flow variables, each of which can yield quantities with units of momentum and energy. Reference [5] introduced an *inviscid criterion* for choosing a proper decomposition to analyze inertial range dynamics and the cascade in such flows. The inviscid criterion stipulates that a scale decomposition should guarantee a negligible contribution from viscous terms in the evolution equation of the large length scales. Here a length scale is "large" relative to the viscous scales. Based

*dzhao5@ur.rochester.edu

on this criterion, Ref. [5] proved mathematically that a Hesselberg [6] or Favre [7,8] decomposition (hereafter Favre decomposition) of momentum and kinetic energy satisfies the inviscid criterion, and then went on to show how an inertial range and a cascade [5,9,10] can exist in variable density high Reynolds number flows. However, Ref. [5] did not prove the uniqueness of the Favre decomposition in satisfying the inviscid criterion, giving only physical arguments on why other decompositions used in the literature are expected to have significant viscous contamination at large length scales and, therefore, are not suitable to study inertial-range dynamics.

Areas of application span many engineered and natural flow systems that have considerable density differences. Large density ratios are often encountered in astrophysical systems, such as in molecular clouds in the interstellar medium which have density ratios ranging from 10^6 to 10^{20} [11–13]. Much higher ratios can be expected in flow systems with gravitational effects, which can lead to the accretion of matter and the formation of ultradense protostars and protoplanets [14]. In high-energy density physics applications performed at national laboratory facilities, such as in inertial confinement fusion experiments, density ratios upward of 10^4–10^5 are frequently encountered [15–17]. In laboratory flow experiments, density ratios of up to 600 have been achieved using different fluids [18,19]. Probably the most ubiquitous terrestrial two-fluid mixing is between air and water, which have a density ratio of 1000. A systematic and rigorous scale-analysis framework is essential to understanding and modeling the multiscale physics of such flows.

In this paper, we shall present a numerical demonstration (1) that the Favre decomposition indeed satisfies the inviscid criterion and (2) that two other decompositions used in the literature do not satisfy the criterion. The results herein apply to flows with variable density due to compressibility effects and to flows of incompressible fluids of different densities. In flows of the second type, which have been called "variable density flows" in the literature [20–23], density is not a thermodynamic variable and acoustic waves are absent. To simplify the presentation, we use the term "variable density" in this paper in reference to both types of flows.

II. DECOMPOSING SCALES

"Coarse graining" or "filtering" provides a natural and versatile framework to understand scale interactions [24–26]. For any field $\mathbf{a}(\mathbf{x})$, a coarse-grained or (low-pass) filtered field, which contains modes at scales $>\ell$, is defined in n dimensions as

$$\overline{\mathbf{a}}_\ell(\mathbf{x}) = \int d^n\mathbf{r} G_\ell(\mathbf{r})\,\mathbf{a}(\mathbf{x}+\mathbf{r}), \tag{1}$$

where $G(\mathbf{r})$ is a normalized convolution kernel and $G_\ell(\mathbf{r}) = \ell^{-n}G(\mathbf{r}/\ell)$ is a dilated version of the kernel having its main support over a region of diameter ℓ. The framework is very general and includes Fourier analysis [27,28] and wavelet analysis [29,30] as special cases with the appropriate choice of kernel $G(\mathbf{r})$. The scale decomposition in Eq. (1) is essentially a partitioning of scales in the system into large ($\gtrsim\ell$), captured by $\overline{\mathbf{a}}_\ell$, and small ($\lesssim\ell$), captured by the residual $\mathbf{a}'_\ell = \mathbf{a} - \overline{\mathbf{a}}_\ell$. More extensive discussions of the framework and its utility can be found in many references [31–39]. In what follows, we shall drop subscript ℓ when there is no risk for ambiguity.

In incompressible turbulence, our understanding of the scale dynamics of kinetic energy, such as its cascade, centers on analyzing $|\overline{\mathbf{u}}_\ell|^2/2$. In the language of Fourier analysis, this is equivalent to analyzing the velocity spectrum $|\widehat{\mathbf{u}}(\mathbf{k})|^2/2$, where $\widehat{\mathbf{u}}(\mathbf{k})$ is the Fourier transform of the velocity field $\mathbf{u}(\mathbf{x})$ (see, e.g., Sec. 2.4 in Ref. [40]).

In variable density turbulence, scale decomposition is not as straightforward. One possible decomposition is to define large-scale kinetic energy as $\overline{\rho}_\ell|\overline{\mathbf{u}}_\ell|^2/2$, which has been used in several studies [41–44]. Another possibility is to define large-scale kinetic energy as $|\overline{(\sqrt{\rho}\mathbf{u})}_\ell|^2/2$, which has also been used extensively in compressible turbulence studies [45–48]. A third decomposition mostly popular in compressible large eddy simulation modeling uses $\overline{\rho}_\ell|\widetilde{\mathbf{u}}_\ell|^2/2$ as the definition of

large-scale kinetic energy, where

$$\widetilde{\mathbf{u}}_\ell(\mathbf{x}) = \overline{\rho\mathbf{u}}_\ell/\overline{\rho}_\ell. \tag{2}$$

This decomposition was apparently first introduced by Hesselberg in 1926 [6] to study stratified atmospheric flows, although it is often associated with Favre [49–52], who first used it in 1958 to analyze compressible turbulence [53]. For a constant density, all these definitions reduce to the incompressible case.

It seems that there is no fundamental *a priori* reason to favor one definition over another. It has been argued that the Favre decomposition is preferred from a "fundamental physics" standpoint since it treats mass and momentum as the elemental variables. While this is certainly a plausible justification, the argument does not identify precisely what physics is missed when utilizing alternate decompositions.

III. THE INVISCID CRITERION

In this paper, we will show that that the non-Favre decompositions can miss the inertial-range physics if density variations are significant. More precisely, we shall show that those alternate decompositions fail to satisfy the *inviscid criterion*.

It is possible to derive the large-scale budgets governing each of those definitions, starting from the original equations [(13) and (14)] of continuity and momentum. Applying the filtering operation to the different combinations of density and velocity forming the three definitions of large-scale kinetic energy [5], one gets

$$\partial_t \overline{\rho}_\ell |\widetilde{\mathbf{u}}_\ell|^2/2 + \cdots = \cdots + \Sigma_\ell^F, \tag{3}$$

$$\partial_t \overline{\rho}_\ell |\overline{\mathbf{u}}_\ell|^2/2 + \cdots = \cdots + \Sigma_\ell^C, \tag{4}$$

$$\partial_t |\overline{(\sqrt{\rho}\mathbf{u})}_\ell|^2/2 + \cdots = \cdots + \Sigma_\ell^K, \tag{5}$$

where the three viscous terms corresponding to the three definitions of large-scale kinetic energy are

$$\Sigma_\ell^F = \widetilde{u}_i\, \partial_j \overline{\sigma}_{ij} = \underbrace{\partial_j[\widetilde{u}_i\, \overline{\sigma}_{ij}]}_{\Sigma_\ell^{F,\mathrm{diff}}} - \underbrace{(\partial_j \widetilde{u}_i)\, \overline{\sigma}_{ij}}_{\Sigma_\ell^{F,\mathrm{diss}}}, \tag{6}$$

$$\begin{aligned}\Sigma_\ell^C &= \overline{\rho}\ \overline{u}_i\, \overline{(\partial_j \sigma_{ij})/\rho} \\ &= \underbrace{\partial_j[\overline{\rho}\ \overline{u}_i\, \overline{\sigma_{ij}/\rho}]}_{\Sigma_\ell^{C,\mathrm{diff}}} - \underbrace{[(\partial_j \overline{u}_i)\, \overline{\rho}\ \overline{\sigma_{ij}/\rho} + \overline{u}_i (\partial_j \overline{\rho})\overline{\sigma_{ij}/\rho} + \overline{u}_i\ \overline{\rho}\ \overline{\sigma_{ij}\partial_j(1/\rho)}]}_{\Sigma_\ell^{C,\mathrm{diss}}},\end{aligned} \tag{7}$$

$$\begin{aligned}\Sigma_\ell^K &= \overline{\sqrt{\rho}\, u_i}\ \overline{\left[\frac{1}{\sqrt{\rho}}\, \partial_j \sigma_{ij}\right]} \\ &= \underbrace{\partial_j(\overline{\sqrt{\rho} u_i}\ \overline{\sigma_{ij}/\sqrt{\rho}})}_{\Sigma_\ell^{K,\mathrm{diff}}} - \underbrace{[\overline{\sqrt{\rho}\, \partial_j u_i}\ \overline{\sigma_{ij}/\sqrt{\rho}} + \overline{u_i\, \partial_j \sqrt{\rho}}\ \overline{\sigma_{ij}/\sqrt{\rho}} + \overline{\sqrt{\rho}\, u_i}\ \overline{\sigma_{ij}\partial_j\left(1/\sqrt{\rho}\right)}]}_{\Sigma_\ell^{K,\mathrm{diss}}}.\end{aligned} \tag{8}$$

Here

$$\sigma_{ij} = 2\mu\left(S_{ij} - \frac{1}{3} S_{kk}\delta_{ij}\right) \tag{9}$$

is the deviatoric (traceless) viscous stress tensor, with the symmetric strain tensor $S_{ij} = (\partial_j u_i + \partial_i u_j)/2$. To keep the presentation simple, we assume a zero bulk viscosity even though all our analysis

here and the proofs in Ref. [5] (see also Ref. [54]) apply to the more general case in a straightforward manner. Superscript "F" stands for Favre, while "C" and "K" denote the lead authors of papers in which those definitions, to our best knowledge, first appeared [41,45]. Terms that transport energy conservatively in physical space, of the form $\boldsymbol{\nabla}\cdot(\dots)$, are denoted by $\Sigma_\ell^{\dots,\mathrm{diff}}$ for viscous diffusive transport. The remaining viscous terms are grouped together as viscous dissipative contributions and denoted by $\Sigma_\ell^{\dots,\mathrm{diss}}$. While this grouping is the most physically sensible, we have also checked that our conclusions hold to different terms within the grouping. In the limit of zero filter length, i.e., in the absence of filtering, all definitions converge:

$$\lim_{\ell\to 0}\Sigma_\ell^{F} = \lim_{\ell\to 0}\Sigma_\ell^{C} = \lim_{\ell\to 0}\Sigma_\ell^{K} = u_i\,\partial_j\sigma_{ij}, \tag{10}$$

$$\lim_{\ell\to 0}\Sigma_\ell^{F,\mathrm{diff}} = \lim_{\ell\to 0}\Sigma_\ell^{C,\mathrm{diff}} = \lim_{\ell\to 0}\Sigma_\ell^{K,\mathrm{diff}} = \partial_j[u_i\,\sigma_{ij}], \tag{11}$$

$$\lim_{\ell\to 0}\Sigma_\ell^{F,\mathrm{diss}} = \lim_{\ell\to 0}\Sigma_\ell^{C,\mathrm{diss}} = \lim_{\ell\to 0}\Sigma_\ell^{K,\mathrm{diss}} = (\partial_j u_i)\sigma_{ij}. \tag{12}$$

It is straightforward to verify that $\Sigma_\ell^{F,\mathrm{diss}}$ is Galilean invariant for any ℓ, whereas $\Sigma_\ell^{C,\mathrm{diss}}$ and $\Sigma_\ell^{K,\mathrm{diss}}$ are not. Since viscous dissipation should satisfy Galilean invariance, this is one indication that the non-Favre decompositions introduce spurious effects to the large-scale dynamics which are inconsistent with the physical role of viscosity. The violation of Galilean invariance would be moot if $\Sigma_\ell^{C,\mathrm{diss}}$ and $\Sigma_\ell^{K,\mathrm{diss}}$ were negligible, but we will show in Sec. IV that they are in fact quite significant. We shall now recap why the Favre scale decomposition satisfies the inviscid criterion, i.e., why $\Sigma_\ell^{F}(\mathbf{x})$ is guaranteed to be negligible everywhere in the domain (not just on average) at length scales ℓ that are large relative to the viscous scales.

Brief recap of the proof

It was shown in Ref. [5] that if third-order moments of the velocity are finite, $\langle|\mathbf{u}|^3\rangle = \frac{1}{V}\int d\mathbf{x}|\mathbf{u}(\mathbf{x})|^3 < \infty$, then it can be rigorously proved that $\Sigma_\ell^{F,\mathrm{diss}}(\mathbf{x})$ is bounded by $O(\mu\,\langle|\mathbf{u}|^3\rangle^{2/3}/\ell^2)$ at every point $\mathbf{x}$. The finiteness of $\langle|\mathbf{u}|^3\rangle^{1/3}$ condition is *almost* as weak as requiring that the flow have finite energy and, therefore, is expected to hold in flows of interest. The type of proof used is standard in real analysis, and for details pertaining to turbulence theory, see Ref. [55] and Appendix A in Ref. [5]. We remark that the derivation of the bound does *not* rely on the presence of turbulence. However, if the Reynolds number based on scale ℓ is small, the bound itself can be non-negligible since ℓ would not be large relative to the viscous scales.

Therefore, at high Reynolds numbers, when $\mu\,u_{rms}^2/\ell^2 \ll 1$, KE at large length scales, defined as $\overline{\rho}_\ell|\widetilde{\mathbf{u}}_\ell|^2/2$ within the Favre decomposition, cannot be directly dissipated by molecular viscosity. Such KE must undergo a cascade or an inviscid nonlinear transfer to smaller scales before it can be efficiently dissipated. A similar bound can be derived for the viscous diffusion term, $\Sigma_\ell^{F,\mathrm{diff}}(\mathbf{x})$, which implies that KE at large length scales does not diffuse due to molecular viscosity.

The idea behind the proof is simple and purely kinematic. A spatial derivative of a filtered field, such as $\boldsymbol{\nabla}\overline{f}_\ell(\mathbf{x})$, has to be bounded in magnitude by $O(f_{rms}/\ell)$. The larger is the length scale, the smaller is the bound as one would expect. Note that the filtered gradients are bounded at every point $\mathbf{x}$ in the domain. For this to hold, it is necessary to be able to commute the gradient with the filtering operation. However, a *nonlinear* term such as $\overline{(g\boldsymbol{\nabla}f)}_\ell$, for general fields $f(\mathbf{x})$ and $g(\mathbf{x})$, cannot be expressed as a gradient of a filtered quantity and, hence, cannot be shown to be bounded. This is especially pertinent to turbulent flows, where it is well known [56–58] that in the limit of large Reynolds numbers (or small viscosity $\mu\to 0$) gradients grow without bound, and, as a result, a term such as $\overline{(g\boldsymbol{\nabla}f)}_\ell$ is expected to diverge, unless there are significant cancellations.

For simplicity, assume for now that viscosity is spatially constant (the proofs in Ref. [5] were extended to the more general case of spatially varying viscosity). It should be straightforward to verify that all derivatives appearing in the Favre viscous terms, $\Sigma_\ell^{F,\mathrm{diff}}$ and $\Sigma_\ell^{F,\mathrm{diss}}$, can be taken outside the filtering operation. It follows that each of $\Sigma_\ell^{F,\mathrm{diff}}(\mathbf{x})$ and $\Sigma_\ell^{F,\mathrm{diss}}(\mathbf{x})$ can be rigorously

bounded by $O(\mu/\ell^2)$, which vanishes in high Reynolds number flows when ℓ is large compared with the viscous cutoff scale [5]. The situation is different for the other two decompositions. For example, the term $\overline{(\sigma_{ij}/\rho)}_\ell$ appearing in Σ_ℓ^C [Eq. (7)] is similar to $\overline{(g\nabla f)}_\ell$ and cannot be rewritten as a gradient of a filtered quantity and, hence, cannot be bounded in the presence of significant density variations. While we are unable to prove mathematically that viscous terms, Σ_ℓ^C and Σ_ℓ^K, do not vanish when ℓ is large, we shall now present numerical evidence that such is the case. From a mathematical standpoint, these different decompositions correspond to different ways to regularizing the equations as was highlighted recently by Eyink and Drivas [54]. They used the inviscid criterion to extend the coarse-graining analysis to internal energy and analyzed the inertial-range dynamics for what they called "intrinsic large-scale internal energy."

In the next section, we test if a scale decomposition satisfies the inviscid criterion by fixing viscosity, μ, and analyzing the viscous contributions as a function of length scale ℓ. This allows us to use a single simulation for each of our tests. Another way to carry out such tests is by analyzing the viscous contributions at a fixed scale ℓ while varying μ. This second way is equivalent to the first in the sense that ℓ is made "larger" relative to the viscous scale by taking $\mu \to 0$ rather than $\ell \to \infty$ as in the first approach. While taking the limit $\mu \to 0$ is still of theoretical and practical interest, it is computationally quite expensive since it requires a series of simulations with a progressively smaller viscosity for every single test.

IV. NUMERICAL RESULTS

In this section, we shall present numerical results from flows of a one-dimensional (1D) shock and the Rayleigh-Taylor instability (RTI) in two and three dimensions. We use the fully compressible Navier-Stokes equations:

$$\partial_t \rho + \partial_j(\rho u_j) = 0, \tag{13}$$

$$\partial_t(\rho u_i) + \partial_j(\rho u_i u_j) = -\partial_i P + \partial_j \sigma_{ij} - \rho\, g\, \delta_{zi}, \tag{14}$$

$$\partial_t(\rho E) + \partial_j(\rho E u_j) = -\partial_j(P u_j) + \partial_j\left[2\mu u_i\left(S_{ij} - \frac{1}{d}S_{kk}\delta_{ij}\right)\right] - \partial_j q_j - \rho u_i\, g\, \delta_{zi}. \tag{15}$$

Here $\mathbf{u}$ is velocity, ρ is density, $E = |\mathbf{u}|^2/2 + e$ is total energy per unit mass, where e is specific internal energy, P is thermodynamic pressure, μ is dynamic viscosity, $\mathbf{g}$ is gravitational acceleration along the vertical z direction, and $\mathbf{q} = -\kappa\nabla T$ is the heat flux with a thermal conductivity κ and temperature T. We use the ideal gas equation of state. S_{ij} is the symmetric strain tensor and σ_{ij} is the viscous stress defined in Eq. (9). In the flows we analyzed, we considered both spatially constant and spatially varying dynamic viscosity and thermal conductivity, as we elaborate below. However, we found that our results are insensitive to this choice.

When calculating viscous terms in Eqs. (6)–(8), the fields are filtered using a Gaussian kernel,

$$G_\ell(|\mathbf{x}|) = \left(\frac{6}{\pi\ell^2}\right)^{n/2} e^{-\frac{6}{\ell^2}|\mathbf{x}|^2}, \tag{16}$$

in dimensions $n = 1,2,3$. This Gaussian kernel form has been used in several prior studies [31,59] due to advantages in numerical discretization (see Ref. [60], p. 30). In this work, we purposefully avoid using a sharp-spectral filter which, for density, yields $\overline{\rho}_\ell(\mathbf{x})$, with Fourier modes larger than $\gtrsim \ell^{-1}$ discontinuously truncated. Such coarse graining of density violates physical realizability since it can have negative values due to the non-positivity of the sharp-spectral filter in x space [5]. In our RT flows, which have no-slip rigid walls at the top and bottom boundaries, filtering near the walls is performed by extending the computational domain in accordance with the boundary conditions. To be specific, beyond the wall, the density field is kept constant (zero normal gradient) and the velocity is kept zero when filtering the RT flows.

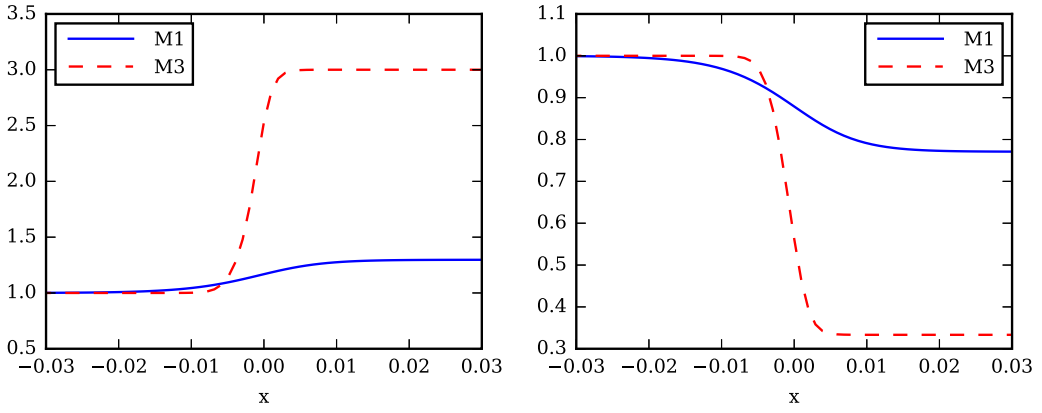

(a)Density (b)Velocity

FIG. 1. Shock profiles at Mach 1.2 (M1) and 3 (M3) in the reference frame of the shock.

A. 1D normal shock

We first test our hypothesis in a simple one-dimensional steady shock solution of Eqs. (13)–(15). Here we shall show that unlike the Favre decomposition, the alternate two decompositions yield a significant viscous contribution at large length scales at a moderate transonic Mach number, which becomes even more pronounced in a Mach 3 shock.

Equations (13)–(15) with zero gravity are solved numerically starting from the Rankine-Hugoniot jump conditions. The solutions are in the shock frame of reference and are shown in Fig. 1. The parameters we consider are in Table I. Zero-gradient boundary conditions (BCs) apply at the boundaries of the our domain. We use subscript "0" for the upstream (preshock) region and "1" for the downstream (postshock) region. In addition to the two cases in Table I, we also analyzed a Mach 3 shock with constant viscosity. The results (see the Appendix) are very similar to those presented here at the same Mach number, indicating that a variable viscosity does not affect our conclusions. It is perhaps worth noting that in the 1D shock context, μ in the viscous stress [Eq. (9)] can be regarded as the sum of dynamic viscosity and three fourths the bulk viscosity [61].

Equations of conservation of mass, momentum, and energy fully determine the postshock flow variables, ρ_1, u_1, and p_1, from their preshock counterparts, ρ_0, u_0, and p_0:

$$\begin{aligned} m_0 &= \rho_0 u_0 = \rho_1 u_1, \\ m_0 V_0 &= \rho_0 u_0^2 + p_0 = \rho_1 u_1^2 + p_1, \\ m_0 I_0 &= \left(\frac{1}{2}\rho_0 u_0^2 + \frac{\gamma}{\gamma-1} p_0\right) u_0 = \left(\frac{1}{2}\rho_1 u_1^2 + \frac{\gamma}{\gamma-1} p_1\right) u_1. \end{aligned} \tag{17}$$

TABLE I. Parameters of the 1D shock solutions shown in Fig. 1. Unlike run M3, M1 uses a spatially constant dynamic viscosity μ_0. Both solutions are for a Prandtl number of unity, $\mathrm{Pr} = \mu C_p/\kappa = 1$. The shock width ℓ_s, which is associated with ℓ_μ, is calculated from the maximum gradient scale length $\ell_s = \max \frac{|u|}{|\nabla u|}$. Unfiltered dissipation $\langle \Sigma^{\mathrm{diss}}_{\ell=0} \rangle$ is given by Eq. (12).

	Ma	Re_0	μ_0	$\mu(\mathbf{x})$	Pr	L	ℓ_s	ℓ_μ	$\langle \Sigma^{\mathrm{diss}}_{\ell=0} \rangle$
M1	1.2	1000	10^{-3}	μ_0	1	1	4.39×10^{-2}	4.36×10^{-3}	1.82×10^{-3}
M3	3	1000	10^{-3}	$\mu_0 T^{0.76}$	1	1	1.07×10^{-2}	1.50×10^{-3}	3.03×10^{-2}

The solution can be normalized by the three dynamical invariants, m_0, m_0V_0, and m_0I_0, which are three independent parameters set as boundary conditions [62]. Fixing a pre-shock Mach number, M_0, is equivalent to fixing the ratio of ram pressure to thermodynamic pressure, $\rho_0 u_0^2/\gamma p_0$, which effectively fixes I_0, leaving two free parameters, m_0 and V_0. In what follows, we shall normalize our results in terms of ρ_0 and u_0.

There are two length scales of interest to us in this problem. The viscous scale of the shock,

$$\ell_\mu \equiv \frac{\mu_0}{\rho_0(u_0 - u_1)} = \frac{\mu_0}{\rho_0 u_0}\left(\frac{\gamma+1}{2}\frac{M_0^2}{M_0^2-1}\right), \tag{18}$$

and a characteristic macroscopic length scale determined from the Reynolds number (which is arbitrary in this simple shock solution) and is independent of the Mach number,

$$L \equiv \frac{\mu_0}{\rho_0 u_0}\mathrm{Re}_0. \tag{19}$$

Their ratio is solely a function of the Reynolds and Mach numbers:

$$\frac{L}{\ell_\mu} = \mathrm{Re}_0\left(1 - \frac{1}{M_0^2}\right)\frac{2}{\gamma+1}. \tag{20}$$

In what follows, we shall define length scale ℓ in relation to the macroscopic scale L due to its independence of M_0. This allows us to compare scales in flows at the same Re_0 but at different M_0.

The dissipation terms, $\Sigma_\ell(\mathbf{x})$ and $\Sigma_\ell^{\mathrm{diss}}(\mathbf{x})$, using the three decompositions at length scale $\ell = L/8$, are plotted as a function of $\mathbf{x}$ in Fig. 2. It shows that at both Mach numbers, the Favre decomposition yields the smallest viscous contribution to the "large-scale" dynamics. We also observe that the discrepancy between the three decompositions increases with higher M_0. As we have discussed, in the limit of zero density gradients, all three decompositions converge, while in the limit of high Mach numbers and increasing density differences, the discrepancy between the three decompositions is expected to grow. Notice that $\Sigma_\ell^{\mathrm{F,diss}}(\mathbf{x})$ and $\Sigma_\ell^{\mathrm{K,diss}}(\mathbf{x})$ are both asymmetric around the shock, which is due to the density weighting.

The viscous dissipation as a function of length scale is plotted in Fig. 3. Here we define wave number as $k = L/\ell$, such that the wave number associated with the shock width is $k_\mu = L/\ell_\mu$ from Eq. (20). The left two panels in Fig. 3 show evidence of significant viscous contamination at intermediate to large length scales within the non-Favre decompositions. The contamination also seems to increase with Mach number. This presents evidence that the two non-Favre decompositions we consider here violate the inviscid criterion and that they are not suitable to analyze inertial-range dynamics in compressible flows. The right two panels show the scaling of the L^∞ norm of $\Sigma_\ell^{\mathrm{diss}}(\mathbf{x})$ for the three decompositions. It shows that $\|\Sigma_\ell^{\mathrm{F,diss}}\|_\infty$ varies as ℓ^{-2} at both Mach numbers and for constant and spatially varying μ, which is consistent with the proof of Ref. [5], because $\|\Sigma_\ell^{\mathrm{F,diss}}\|_\infty$ is the upper bound of the pointwise quantity $|\Sigma_\ell^{\mathrm{F,diss}}(\mathbf{x})|$ and, therefore, the dissipation has to vanish at every point $\mathbf{x}$ at least as fast as ℓ^{-2} for large ℓ.

On the other hand, the non-Favre dissipation terms vary as a ℓ^{-1}. While this is a weaker decay rate than that obtained by a Favre decomposition, it suggests that viscous contributions perhaps do vanish in the limit of large length scales. However, the ℓ^{-1} decay is due to the presence of just one singular structure (the shock) whose effect is diluted by filtering over an ever-wider domain in one dimension. We will present evidence below that this trend does not hold in more complex flows.

B. Two-dimensional (2D) Rayleigh-Taylor instability

Equations (13)–(15) with $g = 1$ are used to conduct five different simulations of the RTI in two dimensions using our code DiNuSUR. We impose no-slip BCs at the top and bottom walls and periodic BCs in the horizontal direction. All five runs were carried out on a $N_x \times N_z = 512 \times 1024$ grid using a pseudospectral solver in the horizontal direction and a sixth-order compact finite

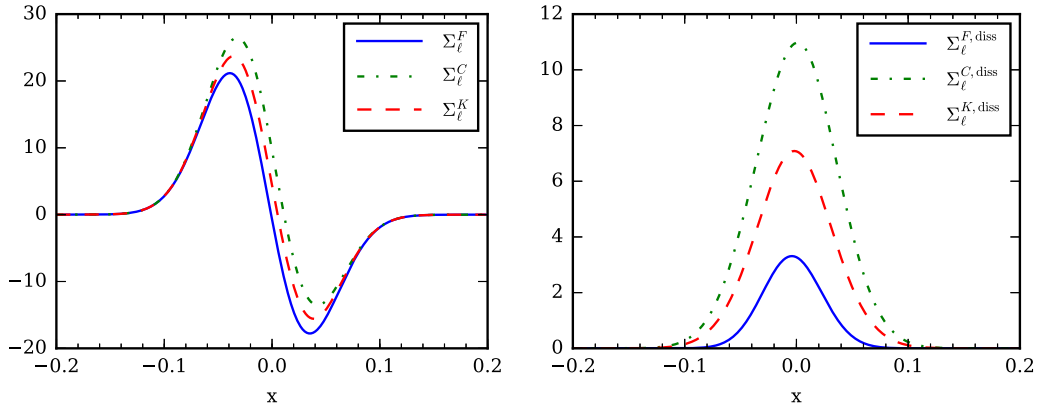

(a)Viscous contribution at L/8

(b)Dissipation at L/8

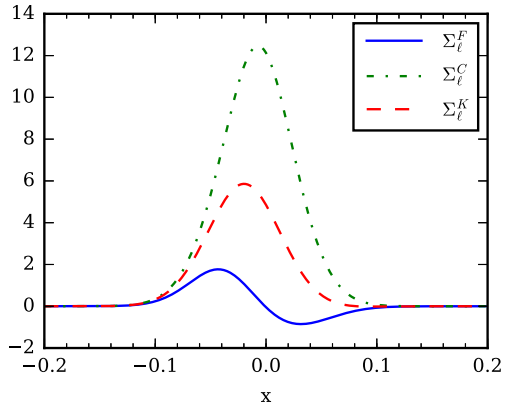

(c)Viscous contribution at L/8

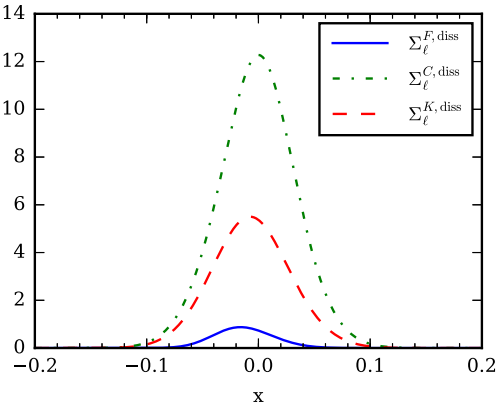

(d)Dissipation at L/8

FIG. 2. Mach 1.2 (top row) and 3 (bottom row). The viscous contributions are calculated at length scale $L/8$. The data are normalized by the unfiltered dissipation. The Favre decomposition yields a smaller viscous contribution at large length scales compared to the other two decompositions. Moreover, the disparity between decompositions increases with Mach number.

difference scheme in the z direction. The physical dimensions of the domain are $L_x \times L_z = 1.6 \times 3.2$. The initial conditions of the simulations are those of a heavy fluid with $\rho_h = 1.0$, filling the top half of the domain in the z direction, over a lighter fluid with density ρ_l in the bottom half. The initial pressure satisfies the hydrostatic equilibrium $dP/dz = -\rho g$, and the initial velocity is zero with velocity perturbation added at the interface. Small amplitude perturbations result in RTI, which evolves until the times shown in Fig. 4, which are the snapshots we analyze. The specific time at which we analyze the flow is not special except in that the flow has to develop sufficiently for the nonlinearities to become significant. We have checked that our conclusions hold at other times (see the Appendix). The snapshots from the five flows we analyze are highly nonlinear (the density modulation amplitude exceeds the perturbation wavelength) but not fully turbulent. The Kolmogorov dissipative length scale in Table II is larger than the grid cell size in all our cases. The Grashof number is slightly larger than unity, which indicates that our simulations may become underresolved at much later times when the flow becomes turbulent [63].

Dynamic viscosity, μ, in some of our simulations was taken to be spatially constant similar to previous studies of Rayleigh-Taylor turbulence [64,65]. In two of our simulations, we also used a temperature-dependent viscosity, $\mu(\mathbf{x}) = \mu_0(T(\mathbf{x})/T_0)^\alpha$, with $\alpha = 0.3$. We have taken α smaller than

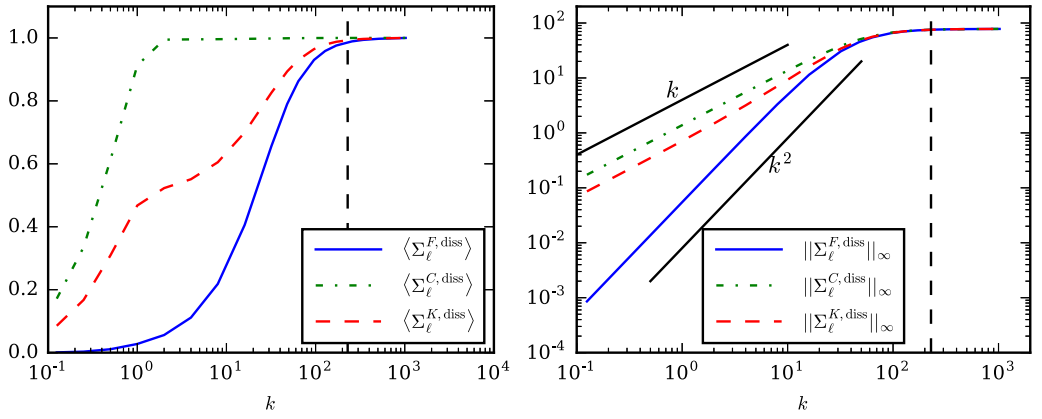

(a)Dissipation average

(b)Dissipation L^∞ log-log

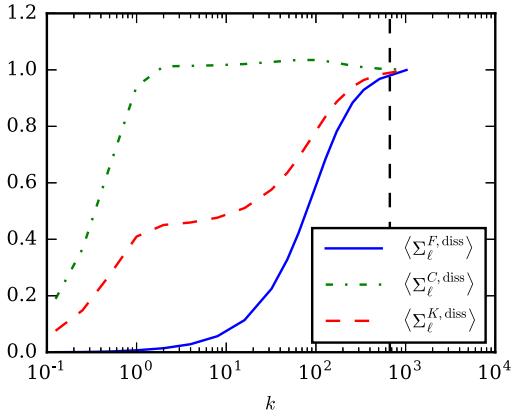

(c)Dissipation average

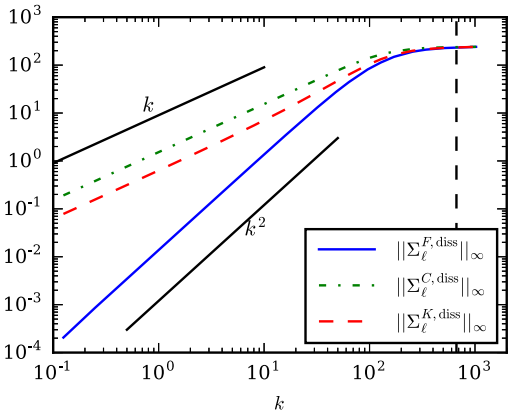

(d)Dissipation L^∞ log-log

FIG. 3. Mach 1.2 (top row) and 3 (bottom row). The figure shows both the average and the maximum dissipation as a function of $k = L/\ell$, and the vertical line in each figure marks the viscous cutoff wave number $k_d = k_\mu = L/\ell_\mu$. Data are normalized by the unfiltered dissipation. Left two panels show how the non-Favre decompositions yield significant viscous contamination at large length scales. Right two panels show that $\Sigma^{F,\mathrm{diss}}$ decays as ℓ^{-2} as proven mathematically, whereas the non-Favre definitions decay at a much slower rate of ℓ^{-1} due to the dilution of the shock's effect in one dimension.

the usual $\alpha = 0.76$, which was computationally too expensive to numerically solve the equations with hot-to-cold temperature ratios that are several orders of magnitude large.

Figure 5 measures the average viscous contribution $\langle \Sigma_\ell \rangle$, which includes dissipation and diffusion effects in flows with increasing density ratios. In these RT flows with zero in-and-out flow boundary conditions, the contribution from diffusive terms, $\langle \Sigma_\ell^{\mathrm{diff}} \rangle$ in Eqs. (6)–(8), is negligibly small (by a factor 10^{-6} or smaller relative to dissipation) on average at all length scales we analyzed. In such complex flows, the L^∞-norm is not a robust metric, unlike in the 1D shock problem of the previous subsection. To gauge the pointwise dissipation and in order to avoid cancellations from the spatial averaging [$\Sigma_\ell^{\mathrm{diss}}(\mathbf{x})$ is not positive definite], we use the L^1-norm as a metric: $\|\Sigma_\ell^{\mathrm{diss}}\|_1 = \langle |\Sigma_\ell^{\mathrm{diss}}| \rangle$.

In the large density ratio simulations, R3 and R4, the flows do not become very turbulent in the course of their development. The viscous terms in all three cases in Fig. 5 exhibit a similar trend with length scale, despite the higher density ratios in R3 and R4. We induce that density variations alone are not sufficient to yield large differences between the three decompositions, but that velocity fluctuations (or velocity gradients) are just as important.

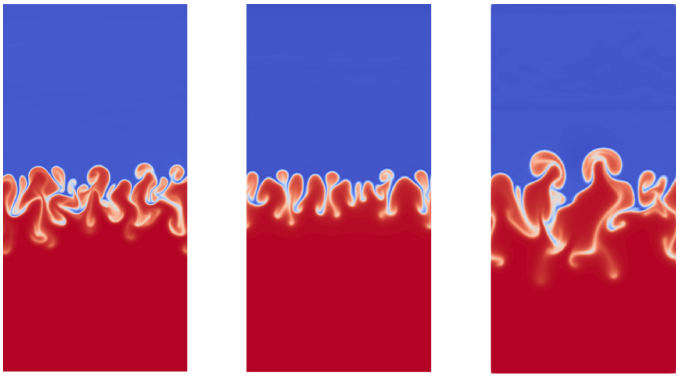

(a)R2 (b)R3 (c)R4

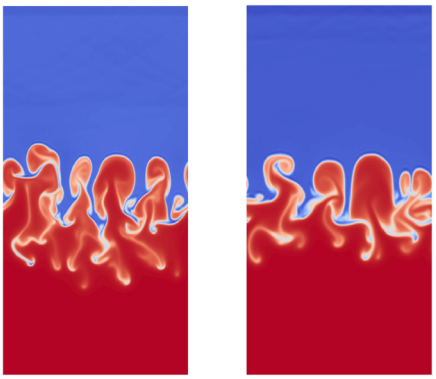

(d)R4vv (e)R4vc

FIG. 4. Density field of 2D buoyancy-driven flows R2–R4 carried out with successively higher initial density ratios (see Table II). Flows R4vv and R4vc in the bottom two panels test the sensitivity of our results to the temperature dependence of viscosity, μ, and thermal conductivity coefficient, κ.

Nevertheless, we still observe marked differences between the three decompositions: (1) $\langle \Sigma_\ell^{\mathrm{C}} \rangle$ is significant and contaminates a wider range of scale before it decays. Moreover, in cases R3 and R4, it becomes negative and grows in magnitude again at the largest scales. (2) While $\langle \Sigma_\ell^{\mathrm{K}} \rangle$ is fairly close

TABLE II. Parameters of the flows shown in Fig. 4. Prandtl number is $\mathrm{Pr}_0 = C_p \mu_0/\kappa_0$, and mesh Grashof number is $\mathrm{Gr} = 2Ag\langle\rho\rangle^2 \Delta x^3/\mu_0^2$, where Δx the grid cell size, g is gravitational acceleration, $A = (\rho_h - \rho_l)/(\rho_h + \rho_l)$ is the Atwood number, and μ_0 is the average dynamic viscosity. The perturbation Reynolds number is $\mathrm{Re}_p = \langle\rho\rangle\lambda\sqrt{Ag\lambda/(1+A)}/\mu_0$, with λ the largest initial perturbation wavelength. The Kolmogorov scale is $\eta = \mu_0^{3/4}/(\epsilon^{1/4}\langle\rho\rangle^{3/4})$, where ϵ is the specific kinetic energy dissipation rate. Gravitational acceleration g is set to 1 in all cases. The temperature range in cases R4vv and R4vc is $T(\mathbf{x}) \in [2.5, 45\,000]$.

	ρ_h/ρ_l	$\langle\rho\rangle$	ρ'_{rms}	$\rho'_{rms}/\langle\rho\rangle$	$\mu(\mathbf{x})$	$\kappa(\mathbf{x})$	Pr_0	Gr	Re_p	$\eta/\Delta x$
R2	10^2	0.501	0.690	1.377	6×10^{-5}	1.2×10^{-4}	1	4.25	528	1.276
R3	10^3	0.489	0.682	1.395	9×10^{-5}	1.8×10^{-4}	1	1.80	344	2.031
R4	10^4	0.482	0.682	1.395	9×10^{-5}	1.8×10^{-4}	1	1.75	339	2.029
R4vv	10^4	0.463	0.641	1.384	$10^{-4} T^{0.3}$	$2 \times 10^{-4}\, T^{0.3}$	1	1.31	293	1.517
R4vc	10^4	0.443	0.615	1.388	$10^{-4} T^{0.3}$	2×10^{-4}	1	1.20	280	1.713

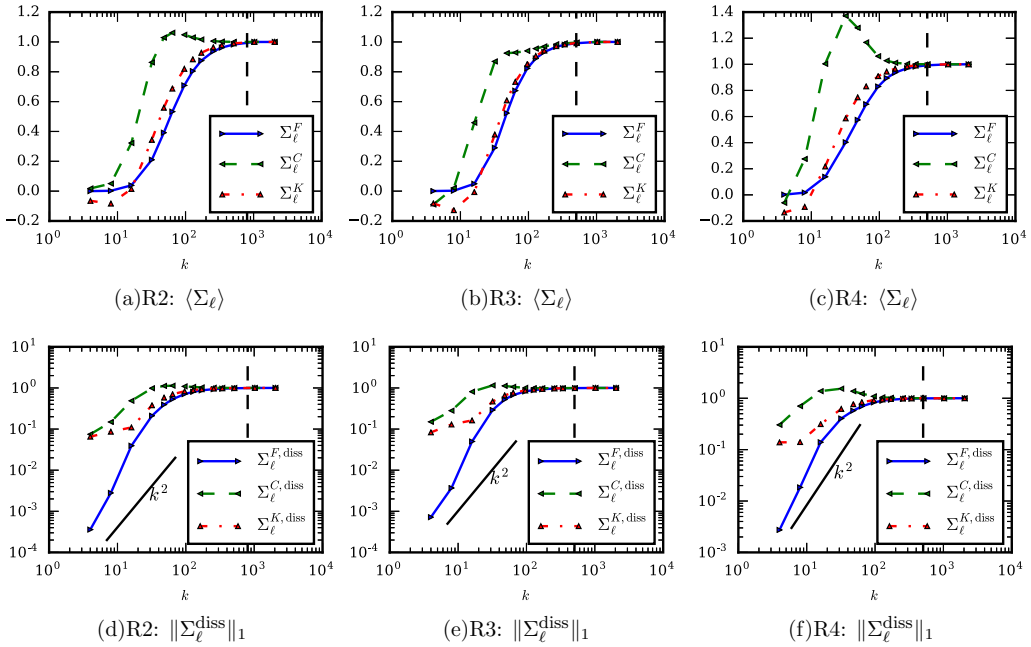

FIG. 5. Comparing the viscous contribution from the decompositions as a function of scale using three flows R2–R4 with increasing density ratio from left to right (see Table II). Horizontal axes are $k = L_z/\ell$, and the vertical line in each figure marks the viscous cutoff wave number $k_d = L_z/\eta$. Top row shows the full viscous contribution $\langle\Sigma_\ell\rangle$. Bottom row shows the L^1 norm scaling of the viscous dissipation, $\|\Sigma_\ell^{\rm diss}\|_1$. Plots are normalized by the unfiltered dissipation. In all cases, the Favre dissipation decays at least as ℓ^{-2} at large scales. The other two definitions do not show a clear decay trend and even become negative on average at the largest scales.

in value to its Favre counterpart over a range of ℓ, it diverges from it and becomes negative (growing in magnitude) at the largest scales in all three cases R2–R4. (3) The clearest distinction between the three quantities is seen when considering $\|\Sigma_\ell^{\rm diss}\|_1$ as a proxy for the pointwise behavior of viscous dissipation. While $\|\Sigma_\ell^{\rm F,diss}\|_1$ decays at least as fast as ℓ^{-2} at large scales, the other two definitions do not show a clear decay trend and are several orders of magnitude larger than $\|\Sigma_\ell^{\rm F,diss}\|_1$, precluding inertial dynamics at those length scales.

The three cases R2–R4 were carried out with a constant viscosity and thermal conductivity. Figure 6 tests the sensitivity of our results to spatially varying $\mu(\mathbf{x})$ and $\kappa(\mathbf{x})$. We observe that the results are qualitatively similar to those in Fig. 5, and that differences between the three decompositions are somewhat enhanced. We also repeated the R4vc case at a lower density ratio $\rho_h/\rho_l = 100$ with similar results (not shown here).

C. Three-dimensional (3D) Rayleigh-Taylor instability

Equations (13)–(15) with $g = 1$ are used to conduct a simulation of a RTI in three dimensions using our code DiNuSUR. We use no-slip BCs at the top and bottom walls and periodic BCs in the horizontal directions. The domain is $L_x \times L_y \times L_z = 1.6 \times 1.6 \times 3.2$. We use a $N_x \times N_y \times N_z = 512 \times 512 \times 1024$ grid, a pseudospectral solver in the horizontal direction, and a sixth-order compact finite difference scheme in the z direction. The initial conditions of the simulations are those of a dense fluid with $\rho_h = 1.0$, filling the top half of the domain in the z direction, over a less dense fluid with $\rho_l = 1/9$ in the bottom half. As in the 2D RT cases, the initial pressure satisfies hydrostatic

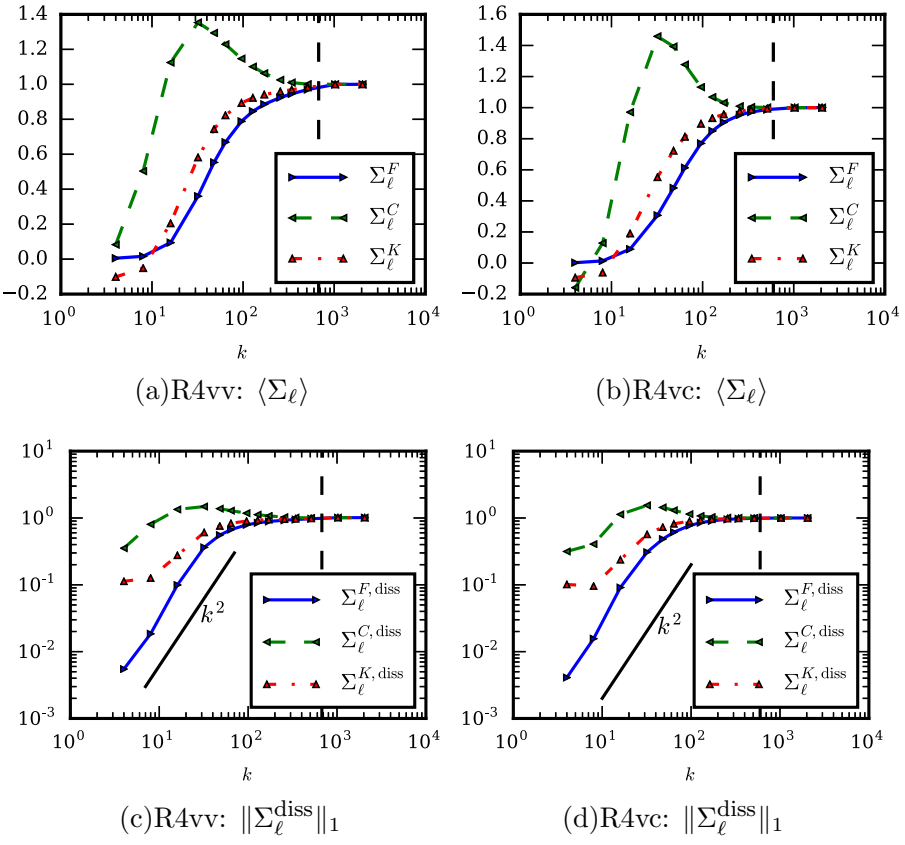

FIG. 6. Similar to Fig. 5. Testing the sensitivity of results to a spatially varying viscosity and thermal conductivity (runs R4vv and R4vc in Table II). Plots are normalized by the unfiltered dissipation. The plots are consistent with those in Fig. 5, showing that our conclusions also hold when $\mu(\mathbf{x})$ and $\kappa(\mathbf{x})$ are spatially varying, as proved in Ref. [5].

equilibrium $dP/dz = -\rho g$. Small-amplitude velocity perturbations result in RTI, which evolves into the fully turbulent regime. Dynamic viscosity, $\mu = 1.35 \times 10^{-4}$, is taken as a constant, although we have shown above that our results pertaining to the inviscid criterion also hold if μ has significant spatial variations.

The estimated Reynolds number of this RT flow is $\mathrm{Re} = \frac{L_x}{\nu}\sqrt{\frac{AgL_x}{1+A}} = 9943$, and the integral length scale is the largest scale that gravity acts on, which is the domain size $L_x = 1.6$. The mesh Grashof number is $\mathrm{Gr} = 2Ag\langle\rho\rangle^2\Delta^3/\mu^2 = 0.822$. The Kolmogorov length scale η is $\eta = \frac{\mu^{3/4}}{\epsilon^{1/4}\langle\rho\rangle^{3/4}} = 7.681 \times 10^{-3}$, where $\epsilon = 4.157 \times 10^{-3}$ is the specific energy dissipation rate. In contrast, the grid size is $\Delta x = 0.0031$, which gives $\eta/\Delta x = 2.478$. A visualization of density at the time we analyze the flow is shown in Fig. 7.

With these data, we analyze the viscous contribution from each of the three decompositions. Figure 8 plots the mean magnitude of dissipation corresponding to three scale decompositions and shows that the Favre definition yields the fastest decay of dissipation at large scales.

While our flow has significant density contrast, with an initial ratio of $\rho_h/\rho_l = 9$, achieving higher ratios in a well-resolved turbulence simulation in three dimensions is computationally challenging [66]. As we mentioned, many flows of interest have very large density ratios. Since the inviscid

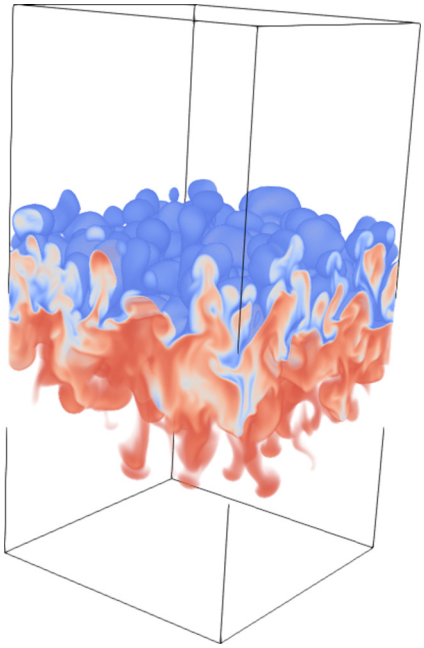

FIG. 7. Visualization of density in the RTI flow at the instant of time we use in our analysis.

criterion is a kinematic result, independent of the dynamics as we have discussed in Sec. III, and in order to highlight differences in the kinematic (or functional) behavior of the viscous terms [Eqs. (6)–(8)] arising from the three decompositions under higher density contrast, we synthetically increase the density contrast in the flow we are analyzing by taking powers of the density $\rho^m(\mathbf{x})$

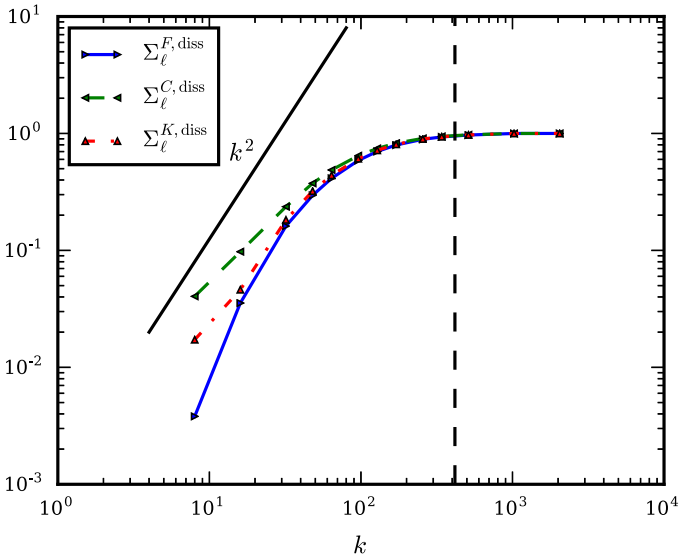

FIG. 8. L^1 norm scaling of the viscous dissipation, $\|\Sigma_\ell^{\mathrm{diss}}\|_1$ using the original 3D RT field in Fig. 7. Plot is normalized by the unfiltered dissipation. In the horizontal axis $k = L_z/\ell$, and the vertical line marks the viscous cutoff wave number $k_d = L_z/\eta$. The Favre dissipation decays the fastest, at least as ℓ^{-2} at large scales.

TABLE III. We consider four cases: the RTI flow shown in Fig. 7 with the original density field, ρ, along with three cases, D2–D8, using synthetic density fields to amplify density gradients. Here $\chi'_{rms} = \langle(\chi - \langle\chi\rangle)^2\rangle^{1/2}$.

	Density χ	$\langle\chi\rangle$	χ'_{rms}	$\frac{\chi'_{rms}}{\langle\chi\rangle}$
D1	ρ	0.554	0.405	0.731
D2	$A_2\rho^2$	0.554	0.546	0.986
D4	$A_4\rho^4$	0.554	0.619	1.118
D8	$A_8\,\rho^8$	0.554	0.654	1.182

with $m = 2,4,8$, as a postprocessing step. ρ^m is then normalized such that the total mass in the domain is the same as in the original flow, $\langle\rho\rangle = A_m\langle\rho^m\rangle$. We then use the three synthetic density fields, $\chi = A_m\rho^m$, to calculate the terms in Eqs. (6)–(8). Table III summarizes the four cases we consider, and Fig. 9 shows the spectra and probability density function (PDF) of the four density fields. The spectra of the three synthetic density fields are physically reasonable in the sense that they are very similar to the spectrum of the original data, although spatial correlations of χ with dynamically relevant fields (e.g., pressure or vorticity) need not be. This justifies using these synthetic density fields to test for the inviscid criterion at the kinematic (or functional) level.

Figure 10 shows the sensitivity of Σ_ℓ from the three decompositions to increasing density variations. We observe that the the Favre decomposition satisfies the inviscid criterion and $\|\Sigma_\ell^{F,\mathrm{diss}}\|_1$ decays at least as fast as ℓ^{-2} for all density fields considered, regardless of the intensity of density variations, in agreement with the results in Ref. [5]. On the other hand, we can clearly see in Fig. 10 that viscous terms in the non-Favre decompositions exhibit a strong sensitivity to density variations. In the presence of strong density variation, $\|\Sigma_\ell^{C,\mathrm{diss}}\|_1$ and $\|\Sigma_\ell^{K,\mathrm{diss}}\|_1$ do not decay at large scales, in violation of the inviscid criterion. We believe that the absence of such a stark sensitivity to density variations in cases R2–R4 of Sec. IV B was probably due to the low level of turbulence in those 2D flows, as we have remarked earlier.

V. SUMMARY

We analyzed the viscous contribution at different length scales of several flows in one, two, and three dimensions and showed that not all scale decompositions are equivalent. In the presence of

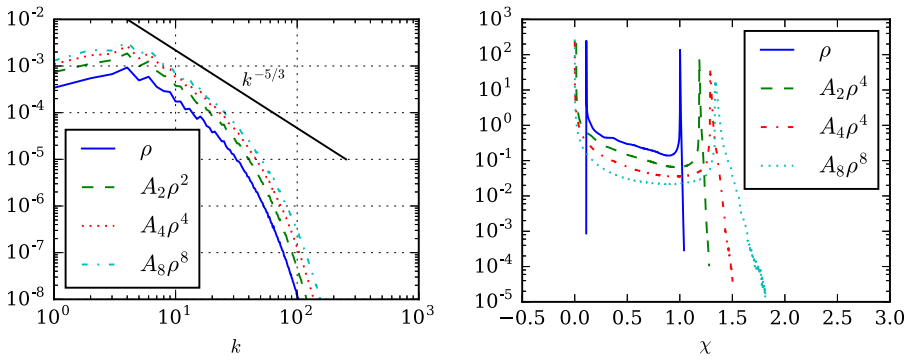

(a)Density spectra (b)Density PDF

FIG. 9. The spectra and PDF of density fields from the snapshot shown in Fig. 7. Spectra are calculated by a 2D Fourier transform in the horizontal directions and then averaging along the z direction, horizontal axis $k = L_z/\ell$. Density spectra in cases D1–D8 have similar scaling but with different fluctuation intensity.

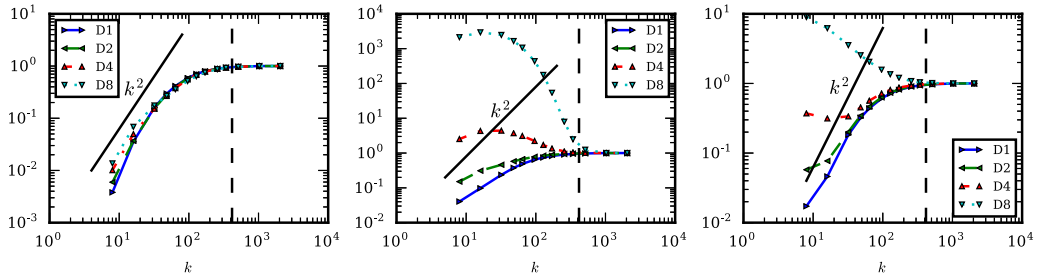

FIG. 10. Sensitivity to increasing density variations: log-log plot of the L^1 norm of dissipation for each decomposition. Horizontal axis are $k \equiv L_z/\ell$, and the vertical line in each figure marks the viscous cutoff wave number $k_d = L_z/\eta$. This shows that the Favre dissipation term decays at least as fast as ℓ^{-2} regardless of the intensity of density variability, unlike the other two decompositions. Note that plots of case D1 are the same as in Fig. 8.

significant density variations, a Favre (or Hesselberg) decomposition satisfies the inviscid criterion by guaranteeing that viscous effects are negligible at large length scales regardless of the intensity of density fluctuations as was shown mathematically in Ref. [5] and demonstrated numerically here.

We also showed how two non-Favre decompositions commonly used in the literature yielded viscous contributions several orders of magnitude greater than that of Favre at large scales. Our results also suggest that these viscous effects may not decay at large length scales in some of the flows we considered, in violation of the inviscid criterion. Therefore, these non-Favre decompositions are not appropriate to analyze inertial-range dynamics in the presence of significant density variations. This has important bearings on attempts to study the energy transfer in variable density turbulence using "triadic interactions" or using $\sqrt{\rho}\mathbf{u}$ as the elemental variable [46,48,67,68]. While triadic interactions are appropriate in incompressible turbulence, where the energy transfer nonlinearity is cubic, they may not be valid for studying energy transfer in variable density turbulence since the scale decomposition associated with such a triadic analysis may not satisfy the inviscid criterion. We remark that the observation of putative power-law scalings of a quantity, such as $|\widehat{\sqrt{\rho}\mathbf{u}}|^2(k)$, is not sufficient to infer that the quantity is undergoing an inertial-range cascade. The results of this paper also have practical modeling implication in showing that viscous terms in LES do not need to be modeled and can be neglected if the resolved scales are large enough.

ACKNOWLEDGMENTS

This work was supported by the DOE Office of Science, Fusion Energy Sciences program Grant No. DE-SC0014318 and the DOE National Nuclear Security Administration under Award No. DE-NA0001944. H.A. was also supported by NSF grant OCE-1259794 and by the LANL LDRD program through Project No. 20150568ER. An award of computer time was provided by the INCITE program, using resources of the Argonne Leadership Computing Facility, which is a DOE Office of Science User Facility supported under Contract DE-AC02-06CH11357. This research also used resources of the National Energy Research Scientific Computing Center, a DOE Office of Science User Facility supported by the Office of Science of the US Department of Energy under Contract No. DE-AC02-05CH11231.

APPENDIX

In Fig. 11 we show results from a 1D normal shock case identical to the M3 case but with a spatially constant viscosity. The results are very similar to those in Fig. 3 above. This is consistent

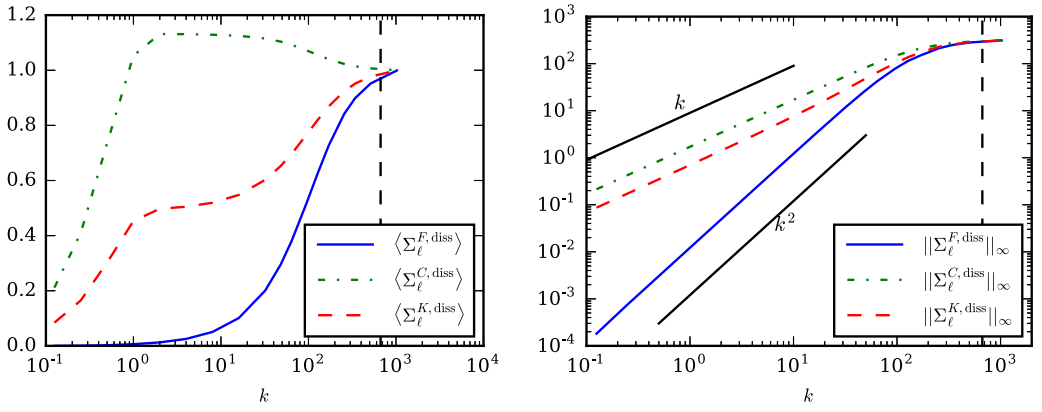

(a)Dissipation average (b)Dissipation L^∞ log-log

FIG. 11. Ma 3 constant spatial viscosity results. Left: average dissipation, right: L^∞ of dissipation. Data are normalized by the unfiltered dissipation, and the vertical line in each figure marks the viscous cutoff wave number $k_d = L/\ell_\mu$.

with our previous assertions that our conclusions are independent of whether or not μ is spatially varying.

In Figs. 12 and 13 we show results from the R3 case of 2D RT flow but at a later time at which the mixing height (average height between bubble and spike) is ≈1.5 times that in Fig. 4, as is visualized

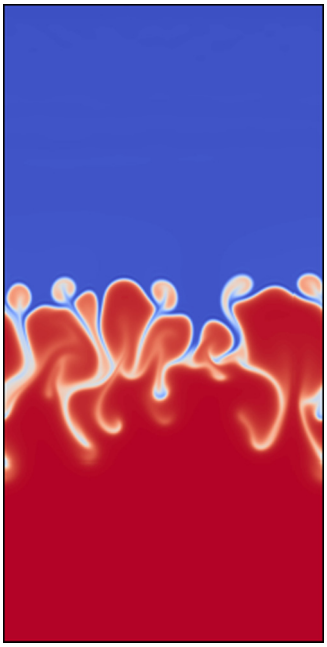

FIG. 12. Visualization of density in the R3 case of 2D RT flow at later time.

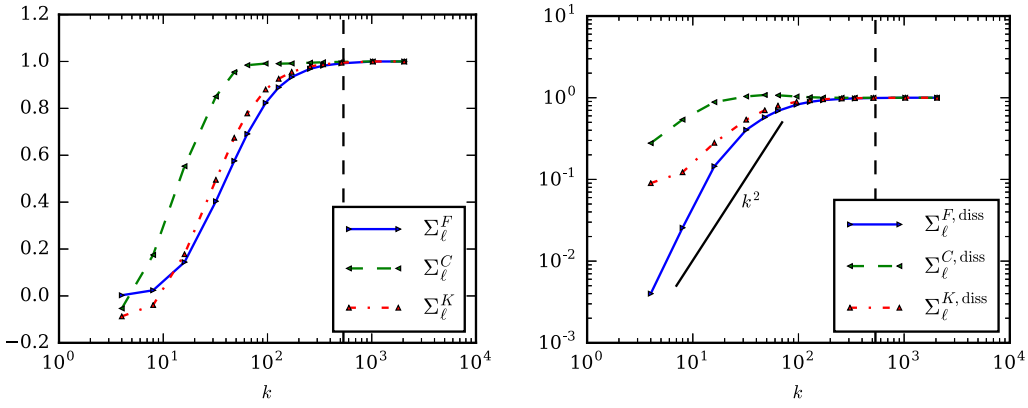

(a)R3: $\langle \Sigma_\ell \rangle$ (b)R3: $\|\Sigma_\ell^{\mathrm{diss}}\|_1$

FIG. 13. The viscous contribution and viscous dissipation of R3 at a later time than that used in Fig. 5 above. Left: average viscous contribution, right: L^1 norm of dissipation. Data are normalized by the unfiltered dissipation, and the vertical line in each figure marks the viscous cutoff wave number $k_d = L_z/\eta$.

in Fig. 12. The results are very similar to those in Fig. 5, showing that the particular snapshots we chose to analyze above in the RT flows are not special and that our results hold in general.

[1] The length scale associated with velocity, $\mathbf{u}(\mathbf{x})$, and that with vorticity, $\nabla \times \mathbf{u}(\mathbf{x})$ for example, will be the same if the scale decomposition (e.g., Fourier transform) commutes with spatial derivatives.

[2] A. Kolmogorov, The local structure of turbulence in incompressible viscous fluid for very large Reynolds' numbers, Akad. Nauk SSSR Dokl. **30**, 301 (1941).

[3] J. R. Herring, R. M. Kerr, and R. Rotunno, Ertel's potential vorticity in unstratified turbulence, J. Atmos. Sci. **51**, 35 (1994).

[4] The potential vorticity regime studied in Ref. [3], in the absence of rotation or stratification, is not geophysically relevant. As the authors of Ref. [3] remark, in the presence of either rotation or stratification, potential vorticity is a predominantly linear quantity that has an inertial range and can therefore cascade.

[5] H. Aluie, Scale decomposition in compressible turbulence, Physica D **24**, 54 (2013).

[6] T. Hesselberg, Die Gesetze der ausgeglichenen atmospharischen bewegungen, Beitr. zur Physik der Atmos. **12**, 141 (1926).

[7] A. J. Favre, J. J. Gaviglio, and R. J. Dumas, Further space-time correlations of velocity in a turbulent boundary layer, J. Fluid Mech. **3**, 344 (1958).

[8] A. Favre, *Problems of hydrodynamics and continuum mechanics*, Statistical equations of turbulent gases (SIAM, Philadelphia, 1969), pp. 231–266.

[9] H. Aluie, Compressible Turbulence: The Cascade and its Locality, Phys. Rev. Lett. **106**, 174502 (2011).

[10] H. Aluie, S. Li, and H. Li, Conservative cascade of kinetic energy in compressible turbulence, Astrophys. J. Lett. **751**, L29 (2012).

[11] A. G. Kritsuk, M. L. Norman, P. Padoan, and R. Wagner, The statistics of supersonic isothermal turbulence, Astrophys. J. **665**, 416 (2007).

[12] C. Federrath, J. Roman-Duval, R. S. Klessen, W. Schmidt, and M. M. Mac Low, Comparing the statistics of interstellar turbulence in simulations and observations, Astron. Astrophys. **512**, A81 (2010).

[13] L. Pan, P. Padoan, T. Haugbølle, and Å. Nordlund, Supernova driving. II. Compressive ratio in molecular-cloud turbulence, Astrophys. J. Lett. **825**, 30 (2016).

[14] P. Hennebelle and E. Falgarone, Turbulent molecular clouds, Astron. Astrophys. Rev. **20**, 55 (2012).
[15] R. S. Craxton, K. S. Anderson, T. R. Boehly, V. N. Goncharov, D. R. Harding, J. P. Knauer, R. L. Mccrory, P. W. McKenty, D. D. Meyerhofer, J. F. Myatt, A. J. Schmitt, J. D. Sethian, R. W. Short, S. Skupsky, W. Theobald, W. L. Kruer, K. Tanaka, R. Betti, T. J. B. Collins, J. A. Delettrez, S. X. Hu, J. A. Marozas, A. V. Maximov, D. T. Michel, P. B. Radha, S. P. Regan, T. C. Sangster, W. Seka, A. A. Solodov, J. M. Soures, C. Stoeckl, and J. D. Zuegel, Direct-drive inertial confinement fusion: A review, Phys. Plasmas **22**, 110501 (2015).
[16] R. Yan, R. Betti, J. Sanz, H. Aluie, B. Liu, and A. Frank, Three-dimensional single-mode nonlinear ablative Rayleigh-Taylor instability, Phys. Plasmas **23**, 022701 (2016).
[17] S. Le Pape, L. F. Berzak Hopkins, L. Divol, N. Meezan, D. Turnbull, A. J. Mackinnon, D. Ho, J. S. Ross, S. Khan, A. Pak, E. Dewald, L. R. Benedetti, S. Nagel, J. Biener, D. A. Callahan, C. Yeamans, P. Michel, M. Schneider, B. Kozioziemski, T. Ma, A. G. Macphee, S. Haan, N. Izumi, R. Hatarik, P. Sterne, P. Celliers, J. Ralph, R. Rygg, D. Strozzi, J. Kilkenny, M. Rosenberg, H. Rinderknecht, H. Sio, M. Gatu-Johnson, J. Frenje, R. Petrasso, A. Zylstra, R. Town, O. Hurricane, A. Nikroo, and M. J. Edwards, The near vacuum hohlraum campaign at the NIF: A new approach, Phys. Plasmas **23**, 056311 (2016).
[18] K. I. Read, Experimental investigation of turbulent mixing by Rayleigh-Taylor instability, Physica D (Amsterdam) **12**, 45 (1984).
[19] G. Dimonte and M. Schneider, Density ratio dependence of Rayleigh-Taylor mixing for sustained and impulsive acceleration histories, Phys. Fluids **12**, 304 (2000).
[20] L. Rayleigh, Investigation of the character of the equilibrium of an incompressible heavy fluid of variable density, Proc. Lond. Math. Soc. **s1-14**, 170 (1882).
[21] D. L. Sandoval, The dynamics of variable-density turbulence, Ph.D. thesis, University of Washington, 1995.
[22] D. L. Sandoval, T. T. Clark, and J. J. Riley, Buoyancy-generated variable-density turbulence, in *IUTAM Symposium on Variable Density Low-Speed Turbulent Flows. Fluid Mechanics and Its Applications*, Vol. 41, edited by L. Fulachier, J. L. Lumley, and F. Anselmet (Springer, Dordrecht, 1997), pp. 173–180.
[23] D. Livescu and J. R. Ristorcelli, Buoyancy-driven variable-density turbulence, J. Fluid Mech. **591**, 43 (2007).
[24] A. Leonard, Energy cascade in large-eddy simulations of turbulent fluid flows, Adv. Geophys. **18**, A237 (1974).
[25] C. Meneveau and J. Katz, Scale-invariance and turbulence models for Large-Eddy simulation, Ann. Rev. Fluid Mech. **32**, 1 (2000).
[26] G. L. Eyink, Locality of turbulent cascades, Physica D (Amsterdam) **207**, 91 (2005).
[27] S. G. Krantz, *A Panorama of Harmonic Analysis* (Mathematical Association of America, CITY, 1999).
[28] H. Aluie and G. Eyink, Localness of energy cascade in hydrodynamic turbulence. II. Sharp spectral filter, Phys. Fluids **21**, 115108 (2009).
[29] C. Meneveau, Analysis of turbulence in the orthonormal wavelet representation, J. Fluid Mech. **232**, 469 (1991).
[30] C. Meneveau, Dual Spectra and Mixed Energy Cascade of Turbulence in the Wavelet Representation, Phys. Rev. Lett. **66**, 1450 (1991).
[31] U. Piomelli, W. H. Cabot, P. Moin, and S. Lee, Subgrid-scale backscatter in turbulent and transitional flows, Phys. Fluids A **3**, 1766 (1991).
[32] M. Germano, Turbulence: The filtering approach, J. Fluid Mech. **238**, 325 (1992).
[33] C. Meneveau and J. O'Neil, Scaling laws of the dissipation rate of turbulent subgrid-scale kinetic energy, Phys. Rev. E **49**, 2866 (1994).
[34] G. L. Eyink, Besov spaces and the multifractal hypothesis, J. Stat. Phys. **78**, 353 (1995).
[35] G. L. Eyink, Exact Results on Scaling Exponents in the 2D Enstrophy Cascade, Phys. Rev. Lett. **74**, 3800 (1995).
[36] S. Chen, R. E. Ecke, G. L. Eyink, X. Wang, and Z. Xiao, Physical Mechanism of the Two-Dimensional Enstrophy Cascade, Phys. Rev. Lett. **91**, 214501 (2003).
[37] H. Aluie and G. Eyink, Scale Locality of Magnetohydrodynamic Turbulence, Phys. Rev. Lett. **104**, 081101 (2010).

[38] L. Fang and N. T. Ouellette, Advection and the Efficiency of Spectral Energy Transfer in Two-Dimensional Turbulence, Phys. Rev. Lett. **117**, 104501 (2016).
[39] H. Aluie, Coarse-grained incompressible magnetohydrodynamics: Analyzing the turbulent cascades, New J. Phys **19**, 025008 (2017).
[40] U. Frisch, *Turbulence: The Legacy of A. N. Kolmogorov* (Cambridge University Press, Cambridge, 1995).
[41] P. Chassaing, An alternative formulation of the equations of turbulent motion for a fluid of variable density, J. Mech. Theor. Appl. **4**, 375 (1985).
[42] D. J. Bodony and S. K. Lele, On using large-eddy simulation for the prediction of noise from cold and heated turbulent jets, Phys. Fluids **17**, 085103 (2005).
[43] G. C. Burton, Study of ultrahigh Atwood-number Rayleigh–Taylor mixing dynamics using the nonlinear Large-Eddy simulation method, Phys. Fluids **23**, 045106 (2011).
[44] M. Karimi and S. S. Girimaji, Influence of orientation on the evolution of small perturbations in compressible shear layers with inflection points, Phys. Rev. E **95**, 033112 (2017).
[45] S. Kida and S. A. Orszag, Energy and spectral dynamics in forced compressible turbulence, J. Sci. Comput. **5**, 85 (1990).
[46] A. W. Cook and Y. Zhou, Energy transfer in Rayleigh-Taylor instability, Phys. Rev. E **66**, 026312 (2002).
[47] J. Wang, Y. Yang, Y. Shi, Z. Xiao, X. T. He, and S. Chen, Cascade of Kinetic Energy in Three-Dimensional Compressible Turbulence, Phys. Rev. Lett. **110**, 214505 (2013).
[48] P. Grete, B. W. O'Shea, K. Beckwith, W. Schmidt, and A. Christlieb, Energy transfer in compressible magnetohydrodynamic turbulence, Phys. Plasmas **24**, 092311 (2017).
[49] A. Favre, Équations statistiques des gaz turbulents: Masse, quantité de mouvement, C. R. Acad. Sci. Paris **246**, 2576 (1958).
[50] A. Favre, Energie totale, énergie interne, C. R. Acad. Sci. Paris **246**, 2723 (1958).
[51] A. Favre, Energie cinétique, énergie cinétique du mouvement macroscopique, énergie cinétique de la turbulence, C. R. Acad. Sci. Paris **246**, 2839 (1958).
[52] A. Favre, Enthalpies, entropie, températures, C. R. Acad. Sci. Paris **246**, 3216 (1958).
[53] These early studies used ensemble averaging or (Reynolds averaging) rather than filtering to decompose scales. There is a one-to-one correspondence in the definitions by replacing the ensemble average operation with the filtering operation wherever it appears.
[54] G. L. Eyink and T. D. Drivas, Cascades and Dissipative Anomalies in Compressible Fluid Turbulence, Phys. Rev. X **8**, 011022 (2018).
[55] G. L. Eyink, Course notes on turbulence theory, http://www.ams.jhu.edu/eyink/OLD/Turbulence_Spring08/notes.html (2007).
[56] K. R. Sreenivasan, On the scaling of the turbulence energy dissipation rate, Phys. Fluids **27**, 1048 (1984).
[57] K. R. Sreenivasan, An update on the energy dissipation rate in isotropic turbulence, Phys. Fluids **10**, 528 (1998).
[58] B. R. Pearson, T. A. Yousef, N. E. L. Haugen, A. Brandenburg, and P. A. Krogstad, Delayed correlation between turbulent energy injection and dissipation, Phys. Rev. E **70**, 056301 (2004).
[59] J. Wang, M. Wan, S. Chen, and S. Chen, Kinetic energy transfer in compressible isotropic turbulence, J. Fluid Mech. **841**, 581 (2018).
[60] V. John, *Large Eddy Simulation of Turbulent Incompressible Flows: Analytical and Numerical Results for a Class of LES Models*, Lecture Notes in Computational Science and Engineering, Vol. 34 (Springer Science & Business Media, Berlin Heidelberg, 2003).
[61] B. M. Johnson, Analytical shock solutions at large and small Prandtl number, J. Fluid Mech. **726**, R4 (2013).
[62] Y. B. Zel'dovich and Yu. P. Raizer, *Physics of Shock Waves and High-Temperature Hydrodynamic Phenomena* (Dover Publications, New York, 2002).
[63] T. Wei and D. Livescu, Late-time quadratic growth in single-mode Rayleigh-Taylor instability, Phys. Rev. E **86**, 046405 (2012).
[64] D. Livescu, J. R. Ristorcelli, M. R. Petersen, and R. A. Gore, New phenomena in variable-density Rayleigh–Taylor turbulence, Phys. Scr., T **2010**, 014015 (2010).

[65] W. H. Cabot and A. W. Cook, Reynolds number effects on Rayleigh-Taylor instability with possible implications for type Ia supernovae, Nat. Phys. **2**, 562 (2006).

[66] D. Livescu and J. R. Ristorcelli, Variable-density mixing in buoyancy-driven turbulence, J. Fluid Mech. **605**, 145 (2008).

[67] C. A. Z. Towery, A. Y. Poludnenko, J. Urzay, J. O'Brien, M. Ihme, and P. E. Hamlington, Spectral kinetic energy transfer in turbulent premixed reacting flows, Phys. Rev. E **93**, 053115 (2016).

[68] D. Sri Praturi and S. Girimaji, The influence of compressibility on nonlinear spectral energy transfer—Part 1: Fundamental mechanisms, Bull. Am. Phys. Soc. **62**, (2017).